# Determination of the structure of $\gamma$-alumina from interatomic potential and first-principles calculations: The requirement of significant numbers of nonspinel positions to achieve an accurate structural model

Gianluca Paglia,[1,2,*] Andrew L. Rohl,[2,†] Craig E. Buckley,[1] and Julian D. Gale[2]

[1]*Department of Applied Physics, Curtin University of Technology, GPO Box U1987 Perth, 6845, Australia*
[2]*Nanochemistry Research Institute, Department of Applied Chemistry, Curtin University of Technology, GPO Box U1987 Perth, 6845, Australia*

We have performed an extensive computational study of $\gamma$-$Al_2O_3$, beginning with the geometric analysis of approximately 1.47 billion spinel-based structural candidates, followed by derivative method energy minimization calculations of approximately 122 000 structures. Optimization of the spinel-based structural models demonstrated that structures exhibiting nonspinel site occupancy after simulation were more energetically favorable, as suggested in other computational studies. More importantly, none of the spinel structures exhibited simulated diffraction patterns that were characteristic of $\gamma$-$Al_2O_3$. This suggests that cations of $\gamma$-$Al_2O_3$ are not exclusively held in spinel positions, that the spinel model of $\gamma$-$Al_2O_3$ does not accurately reflect its structure, and that a representative structure cannot be achieved from molecular modeling when the spinel representation is used as the starting structure. The latter two of these three findings are extremely important when trying to accurately model the structure. A second set of starting models were generated with a large number of cations occupying $c$ symmetry positions, based on the findings from recent experiments. Optimization of the new $c$ symmetry-based structural models resulted in simulated diffraction patterns that were characteristic of $\gamma$-$Al_2O_3$. The modeling, conducted using supercells, yields a more accurate and complete determination of the defect structure of $\gamma$-$Al_2O_3$ than can be achieved with current experimental techniques. The results show that on average over 40% of the cations in the structure occupy nonspinel positions, and approximately two-thirds of these occupy $c$ symmetry positions. The structures exhibit variable occupancy in the site positions that follow local symmetry exclusion rules. This variation was predominantly represented by a migration of cations away from $a$ symmetry positions to other tetrahedral site positions during optimization which were found not to affect the diffraction pattern. This study has provided further insight of the defect structure of $\gamma$-$Al_2O_3$ which is necessary for the understanding and optimization of properties. This work also demonstrates the advantages of prior use of geometric analysis and interatomic potentials to assess a large number of structural possibilities, before striving to achieve high accuracy with DFT on promising cases.

## I. INTRODUCTION

Due to its hardness, abrasion resistance, mechanical strength, corrosion resistance, high surface area, and good electrical insulation, alumina ($Al_2O_3$) is a material of considerable technological and industrial significance.[1,2] It exists in a variety of metastable structures including the $\gamma$, $\delta$, $\eta$, $\theta$, $\kappa$, $\beta$, and $\chi$ aluminas, as well as the stable $\alpha$-alumina phase.[3,4] The phase transformations that occur during the calcination of gibbsite $[Al(OH)_3]$ to $\alpha$-alumina ($\alpha$-$Al_2O_3$) are of fundamental importance in designing ceramic processing procedures, which use partially calcined starting materials. Having transition phases present in feedstock during aluminum production, to affect both the adsorption of hydrogen fluoride and the feedstock solubility in the electrolytic solution, is becoming critical.[5–7] Controversy over the structures of many of the $Al_2O_3$ phases remains. Without correct knowledge of the structural form, research into the properties, dynamics, and applications of these materials will always be less than optimal.

Many studies have been performed on $\gamma$-alumina ($\gamma$-$Al_2O_3$). It has generally been considered to be a cubic spinel, even though tetragonal distortions have been observed.[4,8–20] Tetragonal representations of the structure have recently been proposed.[21–23] Several studies have suggested a departure from the spinel representation of the structure with the occupation of nonspinel site positions.[22–24] It has also been suggested that $\gamma$-$Al_2O_3$ is a dual phase material, consisting of both cubic and tetragonal domains.[25,26] The presence of hydrogen within the structure has also been suggested.[20,27–34] We have provided a more detailed review of the literature of $\gamma$-$Al_2O_3$ elsewhere.[22,23,35,36]

Most computational studies, beginning with the Monte Carlo work of Peri,[37] have examined the surface rather than the bulk structure of $\gamma$-$Al_2O_3$, with particular regard for its Lewis activity and the interactions with reactive species relating to catalytic applications. Some theoretical studies have involved interatomic potential based molecular dynamics simulations, including calculations of the bulk structure.[38,39] The more recent studies were based on cluster models of the surface and utilized *ab initio* quantum-mechanical methods including molecular orbital (MO) theory,[40–42] semiempirical quantum-mechanical calculations,[41,43] Hartree-Fock (HF),[44,45] and density functional theory (DFT).[45–49] Recent DFT studies also used a series of infinitely repeating slabs to model the surface.[50,51]

The unit cell of $\gamma$-$Al_2O_3$ does not have an integer number of aluminium ions, therefore multiple cells are required to simulate the bulk structure with the correct stoichiometry. As computing power has increased, different approaches to simulating the unit cell have been adopted. Interatomic pair potentials are not as computationally expensive as quantum-mechanics-based methods and allow for simulation of larger numbers of atoms. Pair potentials have been used in early molecular dynamics simulations of supercells containing 1440,[52] 3600,[38] and 11 520[39] atoms to examine the bulk structure. More recently, interatomic potentials were used to perform a series of single-point calculations and optimizations of several structural models by Streitz and Mintmire[53] and of 750 000 configurations by Watson and Willock.[54] Both utilized supercells three times the size of the unit cell, i.e., $Al_{64}O_{96}$, to maintain the correct stoichiometry. The earliest use of quantum-mechanics-based techniques involved *ab initio* plane-wave DFT calculations on a 20 atom orthorhombic cell of the asymmetric unit, using local-density approximation (LDA) and norm-conserving pseudopotentials, followed by Monte Carlo simulations on a 1440 atom supercell using a simple potential model.[55] Mo *et al.*[56] examined a series of nonstoichiometric $Al_{21}O_{32}$ cells to approximate $Al_2O_3$, using interatomic pair potentials and more computationally expensive *ab initio* DFT, based on the local-density approximation. Sohlberg *et al.*[57] used *ab initio* DFT within the generalized gradient approximation (GGA) in order to study 14 atom primitive cells with hydrogen incorporated ($HAl_5O_8$). DFT calculations have also been performed on 40 atom supercells containing eight $Al_2O_3$ formula units.[58,59] To our knowledge all previous computational studies on $\gamma$-$Al_2O_3$ have assumed that the structure is a cubic spinel.[60,61]

The results of these theoretical studies are as diverse as the experimental studies. For example, the molecular dynamics studies by Alvarez *et al.*[39,52,62] showed that the bulk structure of $\gamma$-$Al_2O_3$ is relatively well organized and contains no hydrogen but that the surface has many defects. They also observed oxygen to have varied coordination[52] and found penta-[52] and hepta-coordinated[39] Al in addition to octahedral and tetrahedral. Lee *et al.*[55] observed only octahedrally and tetrahedrally coordinated Al. Sohlberg *et al.*[57] determined that hydrogen is present in varying amounts within the bulk structure. However, Wolverton and Hass[58] found hydrogen spinel to be energetically unfavorable and therefore supported an anhydrous bulk structure. They also found cations to migrate to nonspinel positions during optimization. Several studies observed preferential location of cation vacancies on octahedral sites,[52,53,56,58,59] but one determined vacancies to reside on tetrahedral sites.[38]

Yourdshahyan *et al.*[63] have compared the diffraction patterns of their computationally determined $\kappa$-$Al_2O_3$ structural models with experimentally determined patterns, and thereby showed that their simulated structures are close to the real structure. The current work investigates computationally derived $\gamma$-$Al_2O_3$ structures through comparison of both simulated and experimentally determined diffraction patterns. We believe that this is imperative to ensure the plausibility of theoretical models and is a necessary step before a true comparison of properties can be made. It is also the most direct

way to conclusively prove that a simulated structure is consistent with the real average structure.

We investigate the structure of $\gamma$-$Al_2O_3$, using empirical modeling methods and density functional theory. This is preceded by geometric analysis of the structural candidates to reduce the total number of possible structures (over 1 billion) to a tangible number. Although modeling techniques based on interatomic potentials cannot always yield information with regards to subtle relative energetics, they can often produce reasonably accurate structural data in a fraction of the time taken by quantum-mechanical calculations. *Ab initio* calculations of complex structures such as $\gamma$-$Al_2O_3$ can take many weeks of computing time whereas empirical modeling methods typically only involve a few seconds to minutes. This allows for an extensive search of many possible structural candidates to be performed, with minimal prior assumptions being made, before applying high accuracy quantum mechanical methods to a subset of the more favorable configurations. We have previously demonstrated the effectiveness of this approach using $\kappa$-$Al_2O_3$.[36,64] Because tetragonal structures have been reported for $\gamma$-$Al_2O_3$,[21–23] both tetragonal and cubic structural models are investigated here. A major advantage of computational simulations of the structure is that the configuration at the minimum energy provides the precise cation coordinates. While experimental studies yield information on the relative occupancy of the cations for $\gamma$-$Al_2O_3$ these represent only an average distributed over the possible symmetry related positions.

We shall briefly describe the layout of the paper here. The paper contains results from spinel and nonspinel ($c$ symmetry-based) models of $\gamma$-$Al_2O_3$. Section II describes the symmetry and structural characteristics considered, which is encompassed in the geometric analysis used to generate all the possible structural models and reducing that number to tangible quantity for empirical potential optimization. We focus on describing the generation of spinel structural models because these were assessed first and this is how the structure is commonly viewed. The $c$ symmetry-based models are not considered until Sec. IV B. Following the methodology, we describe the parameters used in the interatomic and first principles calculations in Sec. III. This is followed by the results and discussion which first focuses on the findings from the spinel-based models and explains how they do not result in a representative structure of $\gamma$-$Al_2O_3$. The rest of the results and discussion then focusses on the generation of the $c$ symmetry models (Sec. IV B) and the findings from the optimization of these structures from Sec. IV D. Compelling evidence is provided, indicating that the $c$ symmetry models more accurately describe the structure of $\gamma$-$Al_2O_3$ and characteristic features are explained. Results from DFT calculations are described in Sec. IV E, which is followed by the conclusions of the study.

## II. METHODOLOGY

### A. Consideration of structure

The structure of $\gamma$-$Al_2O_3$ is usually considered to be a cubic spinel, ascribed to $Fd\bar{3}m$ space group symmetry.[60,61]

TABLE I. Summary of site positions available for occupation in the cubic $Fd\bar{3}m$ and tetragonal $I4_1/amd$ space groups used to describe the structure of $\gamma$-$Al_2O_3$. Note that the $a$ and $d$ symmetry positions are the spinel site positions that traditional models of $\gamma$-$Al_2O_3$ assume that the cations are restricted to.

| | $Fd\bar{3}m$ | $I4_1/amd$ | Generic label given in this study |
|---|---|---|---|
| | | Octahedral site positions | |
| Wyckoff symmetry position | $16c$ | $8c$ | $c$ symmetry |
| | $16d$ | $8d$ | $d$ symmetry |
| | | Tetrahedral site positions | |
| Wyckoff symmetry position | $8a$ | $4a$ | $a$ symmetry |
| | $8b$ | $4b$ | $b$ symmetry |
| | | $8e$ | $e$ symmetry |
| | $48f$ | | $f$ symmetry |
| | | $16g$ | $g$ symmetry |

The unit cell contains 32 oxygen ions in $32e$ Wyckoff positions, which are approximately close packed in a face-centered cubic (fcc) arrangement. The cation:anion ratio in $\gamma$-$Al_2O_3$ is 2:3, as opposed to 3:4 for spinel structures, so to maintain stoichiometry there must be $21\frac{1}{3}$ aluminum cations in the unit cell. This creates a defect spinel structure due to the vacancies imposed by such an arrangement. The consideration of a spinel structure restricts the aluminum cations to occupying $8a$ (tetrahedral) and $16d$ (octahedral) Wyckoff positions, which are termed the spinel sites. Hence the stoichiometry can be represented as $Al_{21(1/3)}\square_{2(2/3)}O_{32}$, where $\square$ represents a vacancy among the spinel sites. Note that the $Fd\bar{3}m$ space group also possesses other tetrahedral ($8b$ and $48f$) and octahedral ($16d$) site positions.

A tetragonal distortion of the cubic lattice has been reported for several studies of boehmite-derived $\gamma$-$Al_2O_3$.[4,10,13–15,65,66] The tetragonal $I4_1/amd$ space group, a maximal subgroup of $Fd\bar{3}m$, with $a_{cubic} \approx \sqrt{2} \times a_{tetragonal}$, has been suggested to describe the tetragonally distorted structure.[21–23] The $\gamma$-$Al_2O_3$ structure representation provided by $I4_1/amd$ is analogous to the spinel representation except the unit cell contains half the number of atoms. In this space group, the site positions analogous to the spinel sites in its supergroup are $4a$ ($\equiv 8a$) and $8d$ ($\equiv 16d$).[67] The 16 oxygen ions of the unit cell are located in $16h$ Wyckoff positions and the $10\frac{2}{3}$ Al cations are distributed among the spinel sites. As with $Fd\bar{3}m$, the $I4_1/amd$ space group has other site positions available for occupation: $8c$ (octahedral) and $4b$, $8e$, and $16g$ (tetrahedral). Table I provides a summary of the octahedral and tetrahedral positions available in both space group representations.

Here we examine structural possibilities of $\gamma$-$Al_2O_3$ using both the $Fd\bar{3}m$ and $I4_1/amd$ space groups. The room-temperature lattice parameters used for the starting structure candidates were $a=7.911$ Å for $Fd\bar{3}m$,[24] and $a=5.600$, $c=7.854$ Å for $I4_1/amd$.[21]

Hydrogen has also been considered to be part of the bulk structure of $\gamma$-$Al_2O_3$, resulting in a hydrogen-spinel.[28,32–34,51] Zhou and Snyder[24] found only small amounts of hydrogen in $\gamma$-$Al_2O_3$, one OH per unit cell, and specifically ruled out hydrogen-spinel as a structural possibility. Wolverton and Hass[57] found hydrogen-spinel structures to be thermodynamically unstable with respect to boehmite decomposition to an anhydrous defect spinel. These findings are supported by Rietveld analysis of neutron diffraction data, and a range of other experimental techniques, which showed the presence of hydrogen in the crystalline bulk to be unlikely.[22,35] Therefore we do not consider the presence of hydrogen within the bulk crystalline structure candidates examined here.

### B. Generation of spinel-based structural candidates

In order to account for the fractional number of Al ions in the unit cell, supercells were employed which result in larger periodic systems with an integer number of atoms. A $1 \times 1 \times 3$ tetragonal supercell was applied to the cubic $Fd\bar{3}m$ structure and a $2 \times 1 \times 3$ orthorhombic supercell was applied to the tetragonal $I4_1/amd$ structure. The supercells for each structure contain 96 O and 64 Al atoms, i.e., a total of 160 atoms. In this work, the tetragonal and orthorhombic supercells are referred to as the $Fd\bar{3}m$, or cubic, and $I4_1/amd$, or tetragonal, systems, respectively.

Supercells (based on primitive cells) containing as little as 40 atoms have been used to examine $\gamma$-$Al_2O_3$ due to earlier computational restrictions.[58,59] This limits the type of ordered configurations that are possible compared to the larger supercells used here. Larger supercells were adopted because defects are known to be present in $\gamma$-$Al_2O_3$. The presence of a single defect within a smaller cell can result in a high concentration of defects which interact during the periodic calculation.

As the oxygen sublattice of $\gamma$-$Al_2O_3$ is well known,[4] the oxygen ions can be fixed in idealized positions while the possible configurations are considered for the interstitial Al ions. The Al ions are capable of occupying octahedral and/or tetrahedral site positions. The starting structure models assume that 70% of the Al atoms are distributed in octahedral site positions and the remaining 30% are in tetrahedral posi-

tions. This distribution of cations in the structures is based on the NMR spectroscopy and Monte Carlo simulations of Lee *et al.*,[55] and has also been observed in more recent NMR work.[22]

In the starting structure models, the Al ions were restricted to the spinel positions, $8a$ and $16d$ for $Fd\bar{3}m$ and $4a$ and $8d$ for $I4_1/amd$. This approach was adopted because, most researchers have reported cations to be exclusive to these sites and it reduces the number of possible starting structural configurations. The distances between the $a$ and $d$ symmetry positions are greater than the distances between any other pair of site positions. This should, in principle, yield lower starting lattice energies. Also, significant cation migration has been observed in aluminas using interatomic potential calculations.[64] Consequently, if a departure from exclusive spinel site occupation is energetically favorable it may become apparent during optimization.

Based on these assumptions, there are 48 octahedral and 24 tetrahedral site positions available in each supercell to distribute the cations. An occupancy of 70% of the 64 Al ions among the octahedral site positions yields 45 ions. Hence there are $^{48}C_{45}=17,296$ possible arrangements of the Al ions among the octahedral site positions. Likewise, an occupancy of 30% of the 64 Al ions among the tetrahedral site positions yields 19 ions, generating $^{24}C_{19}=42,504$ possible arrangements of these sites. This yields $^{48}C_{45}\times{}^{24}C_{19}=17\,296\times45\,205=735\,149\,184$ total starting structural possibilities for each space group structure under investigation, or a total of $\sim 1.47$ billion configurations overall. A similar approach is used to generate the $c$-symmetry-based (non-spinel) models, described in Sec. IV B.

### 1. Selection criteria

Optimization of each of the structural possibilities even using interatomic potentials was intractable with the available computing facilities. Selection criteria were developed to reduce the $\sim 1.47$ billion possible starting configurations to a manageable number of structures.

The procedure adopted was to reduce the number of starting structural configurations for optimization to those with the most evenly (or sparsely) distributed cation sublattice. This is expected to provide a group of starting structures that have energies that are amongst the lowest of all the possible configurations. The selection criteria were based on examining three different types of nearest neighbors in the cation sublattice:

(i) The number of nearest-neighbor occupied octahedral positions to an occupied octahedral position (*oct-oct*)—for one occupied octahedral position there can be up to six surrounding nearest-neighbor octahedrally coordinated atoms.

(ii) The number of nearest-neighbor occupied tetrahedral positions to an occupied tetrahedral position (*tet-tet*)—for one occupied tetrahedral position there can be up to four surrounding nearest-neighbor tetrahedrally coordinated atoms.

(iii) The number of nearest-neighbor occupied octahedral positions to an occupied tetrahedral position (*tet-oct*)—for one occupied tetrahedral position there can be up to 12 surrounding nearest-neighbor octahedrally coordinated atoms.

TABLE II. Summary of the application of selection criteria to the total number of possible starting structures to obtain a reduced sample pool for optimization. Each starting structure from the reduced sample pool has the lowest mean *oct-oct, tet-tet*, and *tet-oct* nearest neighbors.

Application of *oct-oct* selection criteria to the 17 296 possible arrangements of 45 cations on 48 octahedral site positions

|         | Mean | Number of structures for the $Fd\bar{3}m$ system | Number of structures for the $I4_1/amd$ system |
|---------|------|--------------------|--------------------|
| *oct-oct* | 5.69 | 432 | 816 |
|         | 5.64 | 5472 | 4656 |
|         | 5.60 | 11 296 | 11 728 |

Application of *tet-tet* selection criteria to the 42 504 possible arrangements of 19 cations on 24 tetrahedral sites

|         | Mean | | |
|---------|------|--------------------|--------------------|
| *tet-tet* | 3.58 | 48 | 192 |
|         | 3.47 | 192 | 768 |
|         | 3.37 | 1464 | 3240 |
|         | 3.26 | 7296 | 7536 |
|         | 3.16 | 16 608 | 10 992 |
|         | 3.05 | 11 712 | 11 376 |
|         | 2.95 | 5184 | 8400 |

Application of *tet-oct* selection criteria to the reduced cubic ($11\,296\times5184=58\,558\,564$) and tetragonal ($11\,728\times8400=98\,515\,200$) sample pool of staring structures

|         | Mean | | |
|---------|------|--------------------|--------------------|
| *tet-oct* | 11.53 | 576 | 5760 |
|         | 11.47 | 20 736 | 160 896 |
|         | 11.42 | 306 048 | 1 555 392 |
|         | 11.37 | 2 592 768 | 7 529 664 |
|         | 11.32 | 10 814 400 | 19 057 536 |
|         | 11.26 | 20 957 568 | 28 162 176 |
|         | 11.21 | 17 104 512 | 24 782 112 |
|         | 11.16 | 5 802 624 | 12 985 632 |
|         | 11.11 | 903 168 | 3 773 280 |
|         | 11.05 | 56 064 | 502 752 |

During the generation of the configurations, the number of *oct-oct*, *tet-tet*, and *tet-oct* nearest neighbors for each occupied atom throughout the lattice were determined. These *oct-oct*, *tet-tet*, and *tet-oct* criteria were applied during the generation of the structural possibilities.

In terms of $\gamma$-$Al_2O_3$ described by $Fd\bar{3}m$ symmetry, the number of structure candidates was reduced to 56 064. For the $I4_1/amd$ system structures the reduced number of structure candidates was 502 752. These values represent the number of structures with the most sparsely distributed cation sublattice (i.e., the lowest mean number of nearest neighbors), with respect to all three selection criteria. A summary of the sample pools obtained from the application of the selection criteria is provided in Table II.

The effectiveness of the selection criteria was examined by determining the single point energies (based on the core

TABLE III. Summary of single point energies (i.e., energies prior to optimization) for the structures with the two lowest mean number of nearest-neighbor cations.

| $Fd\bar{3}m$ system | | | |
|---|---|---|---|
| Mean *oct-oct,* *tet-tet,* *tet-oct* | Mean energy (eV) | Maximum energy (eV) | Minimum energy (eV) |
| 5.60, 2.95, 11.11 | −4955.63 | −4829.72 | −4982.59 |
| 5.60, 2.95, 11.05 | −4968.38 | −4915.85 | −4989.80 |
| $I4_1/amd$ system | | | |
| 5.60, 2.95, 11.11 | −4898.22 | −4748.19 | −4934.10 |
| 5.60, 2.95, 11.05 | −4915.07 | −4801.09 | −4944.17 |

potentials) of each set of starting structures with a different mean number of nearest-neighbor cations. Each set of structures exhibits a mean, maximum, and minimum energy less than the sets of structures with higher average numbers of nearest-neighbor cations. Hence it was verified that the selection criteria were successful in providing a set of starting structural configurations for optimization that had the lowest single point energies for the structures scrutinized. Table III provides a summary of the energies for the starting structural configurations for the two lowest mean number of nearest-neighbor cations.

The reduced number of starting structural configurations for the $I4_1/amd$ system was still a formidable quantity to optimize with the available computational facilities and consequently further criteria for reduction were sought. A set of starting structures was randomly selected from the 502 752 most sparsely distributed structural configurations of the $I4_1/amd$ system. The number of starting structural configurations randomly selected was 57 763.

Once the reduced sets of structures were optimized using interatomic potentials, their resulting structural configurations were analyzed. A selected number of structures were then further optimized using first-principles methods. The structures were selected based on energy and cation configuration characteristics. The optimized structures were compared to recently obtained experimental data[22,23] by generating neutron diffraction patterns. This enables determination of the structural configuration(s) that corresponds to a representative structure of γ-$Al_2O_3$. This approach also serves as an example of the approach of using geometric analysis followed by empirical potential methods and more accurate first-principles methods.

## III. COMPUTATIONAL DETAILS

### A. Interatomic potentials

The potential model derived for α-$Al_2O_3$ determined by Catlow *et al.*,[68] based on the Born ionic model, was employed. The model consisted of short-range repulsive interactions, longer-range van der Waals attractive interactions, long-range Coulombic interactions, and atomic polarization.

The first two types of interaction are described by the Buckingham potential,

$$U_{sr}(r) = A_{ij}e^{-r_{ij}/\rho_{ij}} - \frac{C_{ij}}{r_{ij}^6}, \tag{1}$$

where $r_{ij}$ represents the separation distance between ions $i$ and $j$, $A_{ij}$ and $\rho_{ij}$ are parameters describing the repulsion term, and $C_{ij}$ is the dispersion coefficient describing van der Waals attraction. The long-range electrostatic energy was evaluated using the Ewald method.[69,70] Atomic polarization was incorporated for oxygen ions via the core-shell model where a massless shell is coupled to a core by a harmonic force:[71]

$$U_{(\text{core-shell})} = \frac{1}{2}k_{(\text{core-shell})}r_{(\text{core-shell})}^2. \tag{2}$$

The aluminum ion is not polarizable in the model used here.

More accurate structural information can be obtained from interatomic potentials by scaling them to suit cations in specific types of site positions.[72] This approach was not adopted here because it requires prior knowledge of which site positions the cations reside in after minimization. Since we do not know where the cations are precisely located in γ-$Al_2O_3$, it is more sensible to use the same potential for all Al ions and allow for the possibility of cation migration to different sites throughout the structure. It has been shown that the structural information obtained from this approach is relatively accurate and the relative energies of different structures appear to be valid.[64] Moreover, the accuracy is invariably improved once DFT is applied.

Constant volume simulations were performed using conjugate gradients minimization of the total energy. When the gradient norm fell below a given tolerance, the minimization was changed to the rational function optimization[73] (RFO) algorithm to ensure that the final Hessian is positive definite. The software employed for these calculations was the General Utility Lattice Program (GULP).[74]

### B. First-principles calculations

The first-principles calculations were performed with the SIESTA code,[75,76] which implements density-functional theory. The exchange-correlation contribution to the total energy was treated within the generalized gradient approximation (GGA) of Perdew *et al.*[77] Norm-conserving pseudopotentials[78] were used to describe the nonlocal potential due to the core while the valence electrons were described within the framework of LCAO theory. A numerical double-ζ basis set with polarization functions was employed with soft radial confinement. Here the basis set was variationally optimized at the experimental structure of α-$Al_2O_3$.[79] All structural configurations of γ-$Al_2O_3$ were optimized until all remnant forces were less than 0.01 eV Å$^{-1}$, using a mesh cutoff of 200 Ry. These DFT calculations were performed using four **k** points for the $1 \times 1 \times 3$ supercells of the $Fd\bar{3}m$ system and two **k** points for the $2 \times 1 \times 3$ supercells of the $I4_1/amd$ system. Given the size of the supercells this is equivalent to 12 **k** points for each unit cell in both symmetry systems.

## IV. RESULTS AND DISCUSSION

When optimizing using interatomic potentials, the oxygen sublattice, while remaining relatively stable, showed a tendency to become distorted beyond what is observed experimentally. This artifact of high disorder during optimizing with interatomic potentials was also noticed in the study of $\kappa$-$Al_2O_3$,[64] but is more significant in the case of $\gamma$-$Al_2O_3$ because the presence of defects in the supercell means that it is not possible to implement space group symmetry during optimization. However, with the exception of a small number of structures, the oxygen sublattice remained satisfactorily ordered [Fig. 1(b)]. As was the case for $\kappa$-$Al_2O_3$, the implementation of DFT was found to reduce the distortion of the oxygen sublattice. The number of cycles required to achieve optimization with DFT was influenced by the degree of distortion, with greater distortion resulting in longer times before convergence was achieved. Examples of the oxygen sublattice are shown in Fig. 1 and the associated diffraction pattern in Fig. 2. Disorder in the calculated pattern is observed as greater undulation in the background. A more disordered oxygen sublattice typically results in total structure diffraction patterns which exhibit more disorder also [see Fig. 6(d), for example]. In cases of high oxygen sublattice distortion, the deformation is often due to a small number of severely distorted oxygen atoms while the rest of the sublattice remains relatively well ordered.

The converged set of structures, yielded 1161 and 12 573 distinct minimum energies for the $Fd\bar{3}m$ and $I4_1/amd$ systems, respectively. This large number of distinct minima suggests that the energy hypersurface of $\gamma$-$Al_2O_3$ is festooned with local minima and thus it is not surprising that such a disordered structure is observed experimentally. Unlike with $\kappa$-$Al_2O_3$, configurations with equivalent minimum energies (to three decimal places) did not always imply that the structure was the same. Distortions in the oxygen sublattice during the calculations were found to affect the minima. For example, structures were found to have identical Al sublattice configurations, yet different energy due to different distortion in the oxygen sublattice. Structures were also found with identical energy but different Al sublattice configurations.

### A. Structure analysis

Figure 3 illustrates some of the key energetic data obtained from the interatomic potential optimizations. Comparison is made with the energy distribution of the total sample pool and sets of structures, each with a certain cation sublattice characteristic. The percentage of each set of structures that exhibits each configurational characteristic is shown above the energy distribution. A lower energy distribution was obtained for the structures of the $Fd\bar{3}m$ system, indicating greater energetic stability. The majority of structural configurations exhibited 65 to 75% of cations on octahedral site positions and 35 to 25% of cations on tetrahedral positions after optimization, in good agreement with NMR and Rietveld refinements.[22,23] Only 15.4% of the $Fd\bar{3}m$ system structures and 52.8% of the $I4_1/amd$ system structures
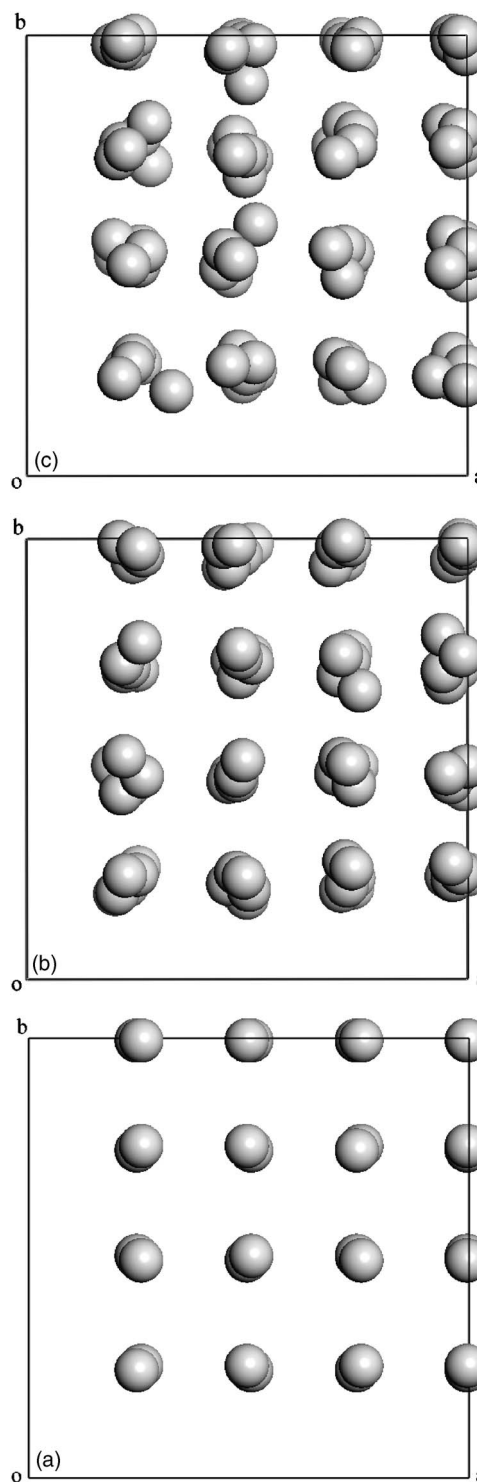


FIG. 1. Examples of the oxygen sublattice, viewed down the $c$ axis. (a) Idealized starting configuration. (b) Typical oxygen sublattice after optimization. (c) Oxygen sublattice displaying significant distortion. These examples were taken from the $Fd\bar{3}m$ system structures.

had cations exclusively on spinel site positions after optimization. These structures were not amongst the lowest-energy configurations, implying that spinel structures (those with Al's solely on spinel positions) are not the most energetically favorable.
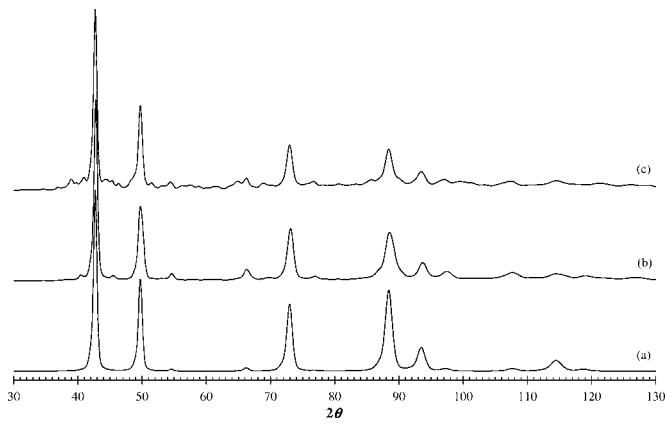
FIG. 2. Examples of neutron diffraction patterns of just the oxygen sublattice. (a) Idealized starting configuration. (b) Typical oxygen sublattice after optimization. (c) Oxygen sublattice displaying significant distortion. These examples were taken from the $Fd\bar{3}m$ system structures. Wavelength=1.66 Å.

The majority of optimized structures exhibited occupancy of nonspinel positions, including the lowest-energy structural configurations. Although less than half of the $I4_1/amd$ system structures possessed nonspinel site occupancy, the mean energy of these structures was less than the structures with only spinel-site positions occupied. Most of the structures with nonspinel occupancy have cations distributed only among $8a/4a$ ($a$ symmetry), $16c/8c$ ($c$ symmetry), and $16d/8d$ ($d$ symmetry) site positions, which were suggested in recent experimental studies.[22,23] The energies of these structures are also lower than those with cations exclusively situated on spinel sites, but the calculated lowest energy structure is not among these structures. Structures that have energies amongst the lowest did have $16c/8c$ sites occupied, but also tended to have other nonspinel sites occupied. These results complement those of Wolverton and Hass[58] who also found occupation of $c$ symmetry positions to occur and that such structures exhibit a lower energy.
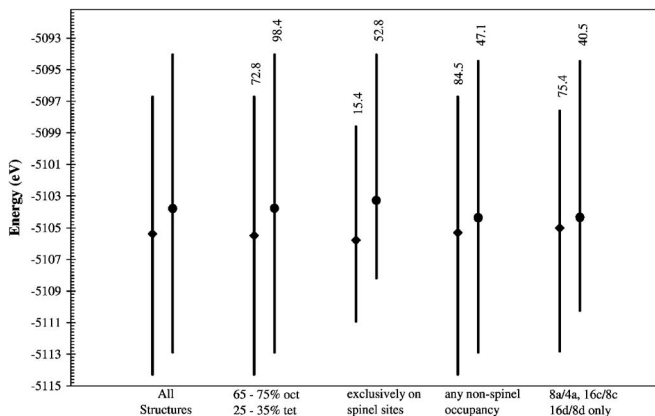


FIG. 3. Key statistics for occupancy and energy distribution of structures obtained from the optimization of the cubic $Fd\bar{3}m$ (♦) and tetragonal $I4_1/amd$ (●) system structures with interatomic potentials. The ♦ and ● symbols indicate the mean energies of the distributions. The value above each energy range is the percentage of the total number of structures that have the configurational characteristic being highlighted.
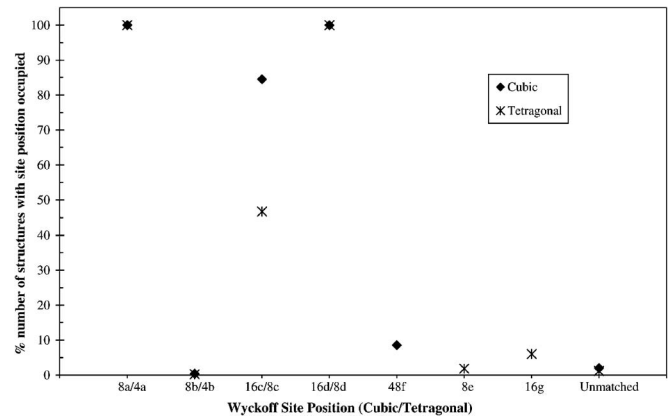


FIG. 4. Occurrence of each type of site position throughout all optimized structures.

In Fig. 4, the number of structures that possess each particular type of site position is indicated. As expected, almost every structure exhibits cation occupancy of $a$ and $d$ symmetry positions. The occurrence of structures with occupied $b$ and $e$ site positions is very infrequent, at less than 1 and 2%, respectively. Cation occupation of $f$ and $g$ symmetry positions is slightly higher representing less than 9 and 6%, respectively. The number of structures with unassigned site positions is low at less than 2%. Unassigned site positions encompasses any non-tetrahedral or octahedral site position, such as the $32e$ site position proposed by Zhou and Snyder.[24] It can also mean any severely distorted site positions that cannot be assigned to any symmetry position. In most cases, the cations in unassigned positions occurred in regions of severe localized disruption of the oxygen sublattice, resulting in the cation being situated beyond the allowed tolerances (up to 0.7 Å away from the idealized starting position) used to determine site occupation. It is therefore concluded that the $32e$ site position, and any nontetrahedral or nonoctahedral site position, are not likely in $\gamma$-Al$_2$O$_3$.

There are a large number of structures with $c$ symmetry positions occupied for both the $Fd\bar{3}m$ and $I4_1/amd$ systems, equal to the number of structures with nonspinel site occupancy (Fig. 4). This is significant, especially given that the cations were restricted to spinel sites in all starting structure models. The statistics highlighted in Fig. 3 provide strong evidence that $c$ symmetry positions are occupied in $\gamma$-Al$_2$O$_3$ and supports the cubic-$16c$ and tetragonal-$8c$ structure models (cubic and tetragonal models which incorporate the $c$ symmetry positions in addition to the spinel sites) derived by us from experimental data.[22] It also suggests that these models are universal for crystalline $\gamma$-Al$_2$O$_3$.

Examination of all optimized structures showed that none of the configurations exhibited a cation composition equivalent to that which is experimentally observed.[22,23] The fractional cation occupancies obtained in the experimental studies ranged between 0.69 and 0.86 $a$ symmetry, 0.30 to 0.45 on $c$ symmetry, and 0.48 to 0.68 $d$ symmetry positions. The limitation of the experimentally derived models is that the occupancies obtained represent an average value distributed over all possible site positions of a particular site. The aim here is to take a closer step towards finding precise cation
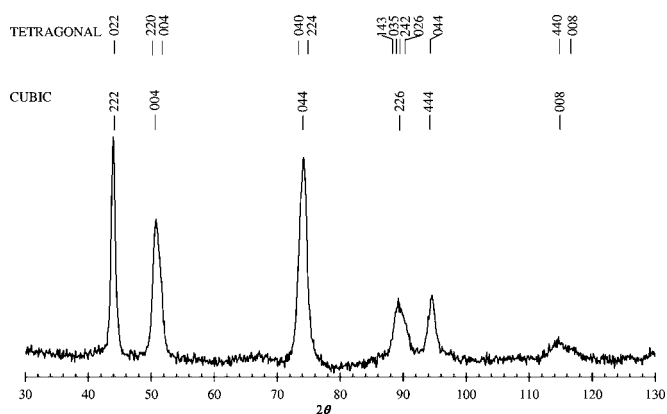
FIG. 5. A typical experimentally measured neutron diffraction pattern obtained from $\gamma$-$Al_2O_3$ prepared from highly crystalline boehmite. This example was measured while heating the material *in situ* at 600 °C (Ref. 22). Miller indices corresponding to the major peaks are shown for both cubic and tetragonal symmetry groups. Wavelength = 1.66 Å.

coordinates of a truly representative structure. In the supercells that have been used in this study, the experimentally determined fractional occupancies equate to Al ions on between (in whole numbers) 17 to 21 *a* symmetry, 14 to 22 *c* symmetry and 23 to 33 *d* symmetry site positions.

Generally, the occupancy of nonspinel symmetry positions after optimization was low; typically less than 5. The closest that any of the optimized structures came to these experimentally determined values[22,23] is no more than four cations on *c* symmetry site positions, in addition to cations on between 17 to 21 *a* symmetry sites and any number of *d* sites, with no other site positions being occupied. There were over twice as many structures of the $I4_1/amd$ system with 17 to 21 *a* symmetry sites and 3 to 4 *c* symmetry sites occupied than for the $Fd\bar{3}m$ system (22 to 9).

None of the optimized structures (or the starting structures) exhibited a diffraction pattern that is characteristic of what is typically observed for $\gamma$-$Al_2O_3$. An experimentally determined diffraction pattern of $\gamma$-$Al_2O_3$ measured from previous work[22] is illustrated in Fig. 5. Anisotropic broadening, synonymous with peak splitting, signifies that the pattern illustrated here corresponds to tetragonally distorted $\gamma$-$Al_2O_3$. If the $\gamma$-$Al_2O_3$ is purely cubic, there is little difference in the diffraction pattern except that no peak anisotropy is observed. Other variations in the diffraction patterns pertain to the degree of crystallinity, which affects the peak intensity and background contribution but does not affect the number of diffraction peaks. Crystallite size and strain may also affect the breadth of the diffraction peaks. Figures 6 and 7 illustrate examples of neutron diffraction patterns generated from the simulated structures. The simulated patterns were generated using Accelrys Materials Studio, using broadening factors derived from experiment.[22] The simulated diffraction patterns have significant peaks which are not present in the experimental pattern. Also the major peaks in the simulated patterns, particularly those at $2\theta \sim 43$, 49, and 73°, do not have the same relative intensities exhibited in the experimental pattern.

DFT calculations also fail to yield a more realistic representation of the structure of $\gamma$-$Al_2O_3$ than the interatomic
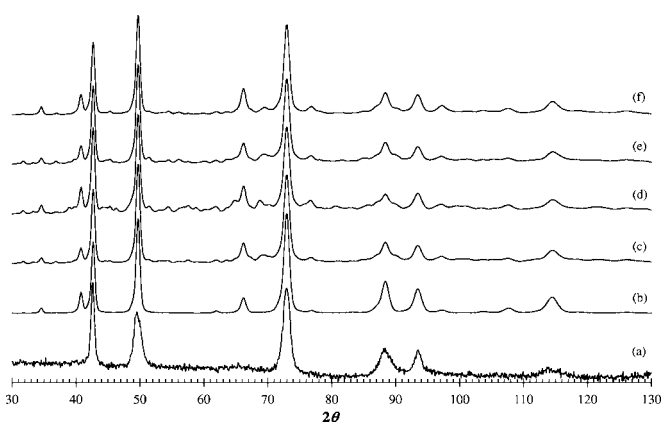


FIG. 6. Examples of simulated diffraction patterns of structures from the $Fd\bar{3}m$ system. (a) Experimental neutron diffraction pattern collected at room temperature from a $\gamma$-$Al_2O_3$ sample prepared by calcining highly crystalline boehmite at 600 °C for seven hours shown for comparison (all experimental diffraction patterns shown in future figures are identical to this) (Ref. 22). (b) Starting structural configuration, with 19 cations on 8*a* positions and 45 cations on 16*d*. The cation configurations in (c)–(f) have the site occupancy on each special symmetry position given in the following order: 8*a*, 8*b*, 16*c*, 16*d*, 48*f*. (c) The lowest energy structure, with 12, 0, 9, 42, 1, (d) 18, 0, 3, 41, 2, (e) 17, 0, 4, 43, 0, (f) 6, 0, 13, 45, 0. Wavelength = 1.66 Å.

potential optimizations. They mainly served to fine tune the structure and reduce the artificial disorder that accompanies the empirical calculations. We therefore conclude that none of the optimized (or starting) structures is representative of the structure of $\gamma$-$Al_2O_3$.

As was seen in the $\kappa$-$Al_2O_3$ study,[64] interatomic potential calculations allow for significant cation migration. As mentioned earlier, the large number of structures exhibiting cation migration to *c* symmetry site positions suggests that Al
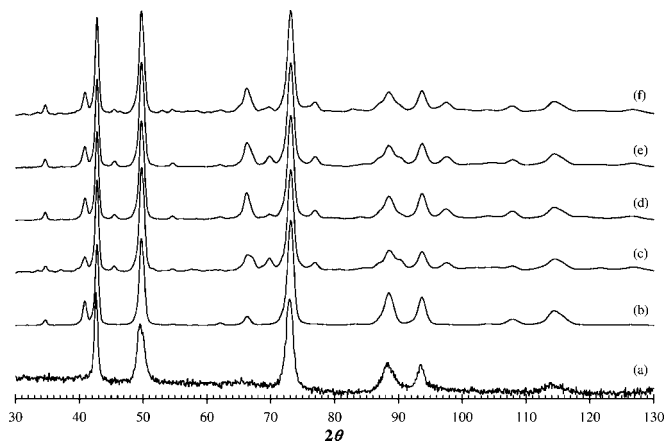


FIG. 7. Examples of simulated diffraction patterns of structures from the $I4_1/amd$ system. (a) Experimental neutron diffraction pattern for comparison. (b) Starting structural configuration, 19 cations on 4*a* positions and 45 cations on 8*d*. The cation configurations in (c)–(f) have the site occupancy on each special symmetry position given in the following order: 4*a*, 4*b*, 8*c*, 8*d*, 8*e*, 16*g*, (c) the lowest energy structure, with 13, 0, 7, 40, 0, 4, (d) 18, 0, 1, 45, 0, 0, (e) 18, 0, 1, 44, 0, 1, (f) 16, 0, 3, 43, 0, 2. Wavelength = 1.66 Å.

ions in these positions are inherent in the structure. However, the discrepancy between the simulated and real structures means that the starting structure models are not close enough to the true structure of $\gamma$-Al$_2$O$_3$ to facilitate the derivation of its representative configuration. This provides compelling evidence that the long held belief of $\gamma$-Al$_2$O$_3$ being a structure where cations are exclusive to spinel site positions can be ruled out. This finding has implications on all previous computational (and most experimental) studies on $\gamma$-Al$_2$O$_3$, i.e., the structural models do not accurately represent the structure of $\gamma$-Al$_2$O$_3$.

### B. More appropriate starting models (nonspinel)

The key to obtaining a representative structure of any material using molecular modeling is to ensure the starting model is as close to the correct configuration as possible. Fortunately, this computational work was accompanied by a parallel experimental study which has provided useful information.[22,23,35,80] A second series of starting structure models were constructed based on the incorporation of cations on $c$ symmetry site positions. Based on the experimental occupancies found,[22] cations were distributed in the supercells as follows; 19 on $a$ symmetry positions (occupancy = 0.792), 17 on $c$ symmetry positions (occupancy = 0.354), and 28 on $d$ symmetry positions (occupancy = 0.583). We refer to these as $c$ symmetry-based structure models.

The starting candidates were generated by fixing the $a$ and $d$ symmetry position cations in idealized positions, as for the oxygen sublattice, and arranging the 17 cations on $c$ symmetry positions in all possible combinations. Three different idealized $a$ and $d$ symmetry cation configurations were chosen for each of the space group symmetry systems. One configuration was obtained by taking the $a$ and $d$ symmetry cations from the lowest-energy structure of the previous set of optimizations to have 19$a$ symmetry cations and 28$d$ symmetry cations, respectively, and set these to idealized coordinates. The other two configurations were chosen by visual inspection to ensure that the $a$ and $d$ symmetry cations were distributed as sparsely and physically reasonably, as possible.

This approach yields $^{48}C_{17} \approx 4.25 \times 10^{12}$ structural possibilities, an immense quantity to optimize. Each idealized configuration was inspected and restrictions were placed on which $c$ symmetry positions Al ions could be situated on, based on nearest-neighbor distances to the pre-established $a$ and $d$ symmetry cations. Care was taken to ensure that the distribution of the $c$ symmetry positions was physically sensible. The $c$ symmetry cations were placed in positions where no $d$ symmetry cation was closer than 2.7 Å. However, all $c$ symmetry positions, for both space group structures, lie in close proximity (1.7 Å) to two $a$ symmetry positions. Given the number of $a$ symmetry cations in the starting structures, it is impossible to avoid placing a $c$ symmetry cation in such a close position to another Al ion. It was therefore decided to ensure that $c$ symmetry cations were placed such that only one $a$ symmetry position is within 1.7 Å, where possible. Application of these restrictions to the six established idealized configurations (three for each space group symmetry system) yielded 19 possible $c$ symmetry
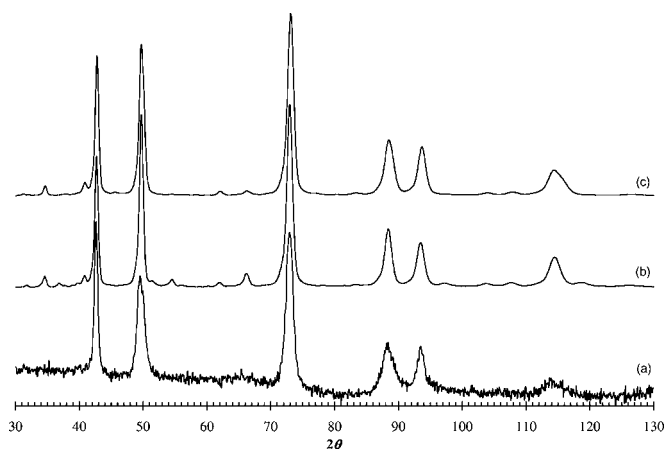


FIG. 8. Examples of diffraction patterns generated from $c$ symmetry-based starting structural configurations. (a) Experimental neutron diffraction pattern for comparison. (b) From the $Fd\bar{3}m$ system and (c) from the $I4_1/amd$ system of structures. Wavelength = 1.66 Å.

positions available for occupation in each structure. This results in $^{19}C_{17} = 171$ possible arrangements for each structure, a total of 513 starting candidates for each space group symmetry system.

Diffraction patterns generated from $c$ symmetry-based starting configurations are illustrated in Fig. 8. These diffraction patterns are significantly different to those from the starting configurations with cations exclusive to spinel positions [Figs. 6(a) and 7(a)]. They are similar to the experimental diffraction pattern (Fig. 5). The peaks at $2\theta \sim 35, 41, 55,$ and $66°$ from the $Fd\bar{3}m$ system diffraction patterns [Fig. 8(b)] are more intense than the equivalent peaks in the $I4_1/amd$ system diffraction patterns [Fig. 8(c)]. This is because the asymmetric unit for the $Fd\bar{3}m$ space group is smaller than that of $I4_1/amd$, and means that the latter can have more atoms in the asymmetric unit. The result is a smaller relative occupancy of the site positions in the $I4_1/amd$ space group (even though on the whole it is the same) and hence means some of the equivalent peaks will be less intense.

The smaller peaks at $2\theta \sim 35, 41, 55,$ and $66°$, and other peaks of similar or lesser intensity, are largely concealed in the experimental pattern by the background contribution, particularly in the lower $2\theta$ range. In the case of the simulated diffraction pattern peaks at $2\theta \sim 62$ and $66°$ there is a corresponding broad hump in the experimental pattern. The cubic diffraction pattern also exhibits reduced intensity of the peak at $2\theta \sim 43°$. Discrepancies in the relative intensities of the three most intense peaks are discussed later.

### C. Oxygen sublattice distortion for $c$ symmetry-based structures

Distortion of the oxygen sublattice was far more severe during optimizations of the $c$ symmetry-based structures, making convergence difficult to achieve. This higher disorder is due to the close proximity of the $c$ and $a$ site positions.
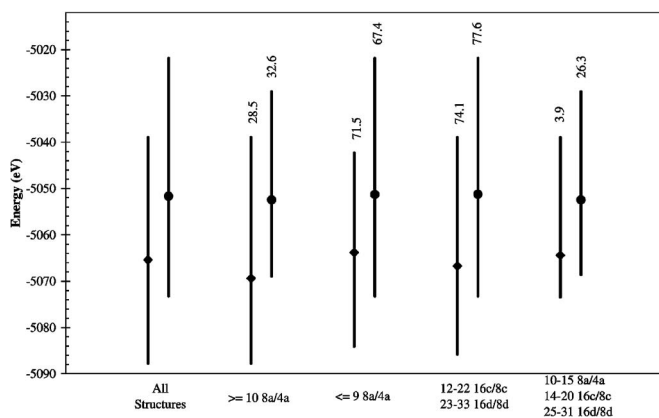
FIG. 9. Key statistics from optimizations of $c$ symmetry-based structural configurations of the cubic $Fd\bar{3}m$ ($\blacklozenge$) and tetragonal $I4_1/amd$ ($\bullet$) system structures with interatomic potentials. The $\blacklozenge$ and $\bullet$ symbols indicate the mean energies of the distributions. The value above each energy range is the percentage of the total number of structures that have the configurational characteristic being highlighted.

It was therefore decided to apply a harmonic restraint to the oxygen sublattice so that the oxygen ions remain confined close to their initial starting positions:

$$E = \frac{1}{2}k(r - r_0)^2. \qquad (3)$$

Here $k$ is the spring constant (which can be varied) used to dictate how much flexibility the oxygen sublattice ions are given to move about their original positions, $r_0$ is the initial ion position and $r$ is the ion position during optimization. This approach goes part of the way to enforcing symmetry during optimization and the degree of distortion in the oxygen sublattice was thereby significantly reduced. Structures from the original set of spinel-based model configurations were also optimized to verify that restraining the oxygen sublattice does not adversely affect the cation configuration.

After optimization of the $c$ symmetry based structures, selected structures were then reoptimized with the restraint on the oxygen sublattice removed. The oxygen sublattice was found to remain well-ordered to the same degree as for the spinel-based structures. Subsequent optimization using DFT further improved the order and the oxygen sublattice was found to be very similar for all structures.

### D. Results from optimization of $c$ symmetry-based structures

The key results from optimization of the $c$ symmetry-based structures are summarized in Fig. 9 and Table IV. As with the previous optimizations, the structures of the $I4_1/amd$ system have higher mean, minimum, and maximum energies than the $Fd\bar{3}m$ system. The higher energy of these structures compared with the spinel-based structures (Fig. 3) is an artificial effect caused by the harmonic restraint placed on the oxygen sublattice; when DFT is performed the energies fall within a similar range. Also, for the characteristics highlighted in Fig. 9, the differences in the mean energies

were smaller for the $I4_1/amd$ system. A greater range in the optimized energies was observed compared with the structures where cations were initially placed on spinel site positions, reflecting the higher amount of overall cation migration experienced for the $c$ symmetry-based structures during optimization. The majority of structures exhibited an even distribution of cations throughout the optimized supercells, maintaining approximate $Al_2O_3$ stoichiometry in each subcell. It can be seen from Table IV that the average occupancy of nonspinel positions is 42 and 45% for the $Fd\bar{3}m$ and $I4_1/amd$ systems, respectively, and approximately two thirds of these occupy $c$ symmetry positions.

After optimization, every structure in both the $Fd\bar{3}m$ and $I4_1/amd$ symmetry systems possessed cation occupation of non-$a$-, -$c$-, or -$d$ symmetry site positions. The nonspinel site occupancy was much higher than for the optimized structures derived from spinel-based starting models where it was rare to have more than five cations in any nonspinel symmetry position. There were no cations in unassigned (nontetrahedral or octahedral) site positions. The cation migration predominantly involves movement of cations away from $a$ symmetry positions to other tetrahedral site positions of lower symmetry. The average number of cations in $a$ symmetry positions after optimization is 8 and 9 for the $Fd\bar{3}m$ and $I4_1/amd$ systems (Table IV), respectively, representing average occupation of 33 and 38%. Most of the cation migration was towards the $48f$ symmetry positions in the $Fd\bar{3}m$ system structures. For the $I4_1/amd$ system the cations were distributed relatively evenly among all the lower symmetry tetrahedral site positions.

The migration to other tetrahedral sites is supposedly due to repulsion between cations in $a$ and $c$ symmetry positions, which are within 1.7 Å of each other in the starting configurations. Cations migrating away from $a$ symmetry positions therefore tend to occupy other tetrahedral positions with fewer $c$ and $d$ symmetry positions nearby.

The cation migration observed in the modeling of the structures exhibits a logical pattern. Locally, symmetry exclusion rules are obeyed such that if two positions are occupied within a region, nearest neighbor positions are not occupied. The cation migration away from $a$ symmetry positions is required for these exclusion rules to be obeyed. When these exclusion rules are obeyed, longer-range ordering results such that positions that are occupied in one subcell of a supercell are not necessarily occupied in the next. There are, for example, many cases where alternate subcells have virtually the same cation configuration, with the separating subcell exhibiting a completely different configuration.

The migration away from $a$ symmetry positions means that the closest structural configurations to the starting configurations had between $10-15$ $a$, $14-20$ $c$, and $25-31$ $d$ symmetry sites occupied, representing a variation from the starting configuration of up to 47.4, 1.7, and 1.1%, respectively. Only 20 structures of the $Fd\bar{3}m$ system and 135 of the $I4_1/amd$ system lie within this range (Fig. 9). None of these were among the lowest energy structures. However, there is comparatively little migration away from the octahedral, $c$ and $d$ symmetry, site positions. For about three quarters of

TABLE IV. Summary of the distribution of cations amongst the possible site positions for all 513 optimized structures of each symmetry system investigated. For each type of Wyckoff symmetry position, the table provides the proportion of structures that have cations occupied in each type of site. The minimum and maximum number of cations occupied in each type of position out of all the structures, the average cation occupation for all the structures, and the $2\sigma$ range are also provided. The $2\sigma$ range shows the cation occupation range encompassing 90% of structures with a particular type of site position occupied. The table also indicates the number on each type of symmetry position in the starting configuration for comparison.

| Wyckoff symmetry position | % structures with position occupied | Possible positions per supercell | Starting positions | Minimum positions occupied | Maximum positions occupied | Average (site occ.) | $2\sigma$ range (site occ.) |
|---|---|---|---|---|---|---|---|
| | | | $Fd\bar{3}m$ system | | | | |
| 8a | 100 | 24 | 19 | 1 | 15 | 8 (0.333) | 3–14 (0.125–0.583) |
| 8b | 19 | 24 | 0 | 0 | 4 | 1 (0.042) | 1 (0.042) |
| 16c | 100 | 48 | 17 | 6 | 28 | 17 (0.375) | 10–24 (0.210–0.500) |
| 16d | 100 | 48 | 28 | 24 | 36 | 29 (0.583) | 25–32 (0.521–0.667) |
| 48f | 100 | 144 | 0 | 3 | 17 | 9 (0.062) | 5–13 (0.035–0.090) |
| | | | $I4_1/amd$ system | | | | |
| 4a | 100 | 24 | 19 | 1 | 15 | 9 (0.375) | 6–14 (0.250–0.583) |
| 4b | 84 | 24 | 0 | 0 | 7 | 2 (0.083) | 1–3 (0.042–0.125) |
| 8c | 100 | 48 | 17 | 9 | 31 | 20 (0.417) | 14–23 (0.292–0.479) |
| 8d | 100 | 48 | 28 | 17 | 33 | 26 (0.542) | 23–33 (0.479–0.688) |
| 8e | 98 | 48 | 0 | 0 | 10 | 4 (0.083) | 1–6 (0.021–0.125) |
| 16g | 97 | 96 | 0 | 0 | 9 | 3 (0.031) | 1–5 (0.010–0.052) |

the structures, the octahedral sites remain within 2.9% of their initial occupancy (Fig. 9). These structures exhibit the same range in energies as the total sample pool, but have a lower mean energy.

Irrespective of the differences between the structural configurations, most of the simulated diffraction patterns generated from the optimized structures have similar appearance for both space group systems. Furthermore, they do not differ significantly from the diffraction patterns of the starting structures. Examples of the simulated diffraction patterns obtained are presented in Figs. 10 and 11. These diffraction patterns also provide an excellent match with experimentally obtained diffraction patterns for $\gamma$-Al$_2$O$_3$ (Fig. 5). (An experimentally obtained diffraction pattern has been overlayed in Figs. 10 and 11 for more direct comparison.)

It is clear from the optimizations that the migration of cations away from $a$ symmetry positions does not affect the pattern significantly (Figs. 10 and 11). The most important

factor in maintaining a diffraction pattern that is close to experiment is the presence of a sufficient number of occupied $c$ symmetry positions. Secondly, a reasonably consistent cation distribution on octahedral sites is required. Only in cases where the structures exhibited significant cation migration away from $c$ symmetry positions did the calculated diffraction patterns show noteworthy divergence from the experimental ones. This occurred for structures where the number of cations on $c$ symmetry positions was less than 10, of which there were 9 structures total for both symmetry systems, showing increased intensity of the peaks at $2\theta$ $\sim$41 and 66°. Irrespective of which site positions are occupied, the ratio of octahedral to tetrahedral cations in the optimized structures is consistently around 2.33:1, although more structures achieve this for the $I4_1/amd$ system.

Except for the nine structures with less than ten cations on $c$ symmetry positions, the only significant discrepancies between the experimental and simulated diffraction patterns lie
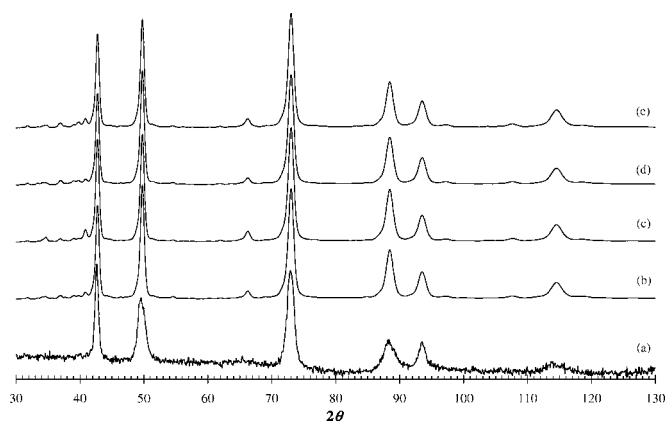
FIG. 10. Examples of simulated diffraction patterns from *c* symmetry-based structures of the $Fd\bar{3}m$ system. (a) Experimental neutron diffraction pattern for comparison. (b) Closest configuration to starting arrangement (therefore with least amount of non-*a*, -*c*, and -*d* symmetry positions), with 11, 0, 16, 31, 6 (cations on 8*a*, 8*b*, 16*c*, 16*d*, and 48*f* site positions, respectively), (c) 14, 0, 11, 34, 5, (d) 8, 0, 9, 28, 19, (e) 10, 0, 13, 31. Wavelength=1.66 Å.

in the relative peak intensities. In the simulated patterns, the peaks at $2\theta \sim 51$, 73, and 89° are generally more intense than the corresponding peaks in the experimentally measured diffraction pattern. These discrepancies are partly due to preferred orientation in the experimental material. This provides us with a possible answer to the observed discrepancies between diffraction data and the Rietveld calculated pattern, particularly at $2\theta \sim 44°$, in previous work;[22,23] namely the inability of the Rietveld code used to adequately model preferred orientation. As with the starting structures, the smaller peaks, at $2\theta \sim 35$, 41, 55, and 66°, are largely concealed in the experimental pattern by the background contribution.

It should be noted that the disproportionately high intensity of the peak at $2\theta \sim 89°$ in the simulated diffraction patterns from interatomic potential optimization (of both the $Fd\bar{3}m$ and $I4_1/amd$ systems) is due to the restrictions imparted by the harmonic restraint on the oxygen lattice. When the structures are optimized using DFT (Figs. 12 and 13) the peak achieves an intensity comparable to that observed experimentally. The peak at $2\theta \sim 44°$ has a fairly consistent intensity ratio when compared to the other main peaks for all the simulated diffraction patterns in the $Fd\bar{3}m$ system, but not for the $I4_1/amd$ system. It can be seen from Figs. 11(c) and 11(e) that the relative intensities of the peak at $2\theta \sim 44°$, when compared to the peaks at 51 and 73, approaches that observed in the experimental diffraction patterns. Examining the Miller planes corresponding to the peak at $2\theta \sim 44°$ in the modeled structures (222 for cubic symmetry and 022 for tetragonal symmetry) indicates a difference in the type of species present. The 222 plane (226 in the $1 \times 1 \times 3$ supercell) is predominantly composed of oxygen ions, whereas the 022 plane (026 in the $2 \times 1 \times 3$ supercell) also contains a substantial number of cations. The average density of occupied positions on the 022 plane in the modeled $I4_1/amd$ system structures is also higher. Hence the simulated structures from the $I4_1/amd$ system are more representative of the experimental structure as the 022 peak from modeling reflects experiment more closely.
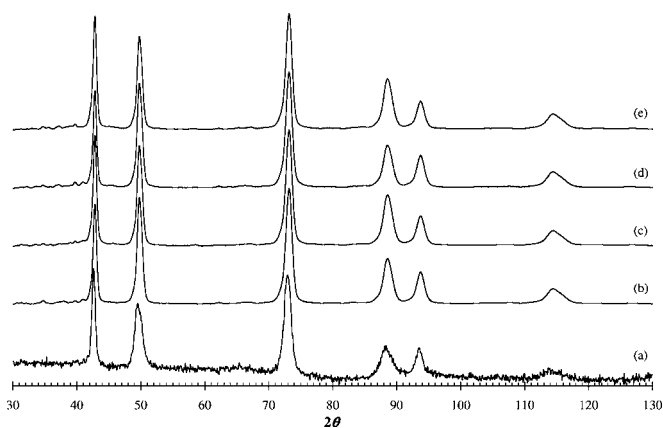


FIG. 11. Examples of simulated diffraction patterns from *c* symmetry-based structures of the $I4_1/amd$ system. (a) Experimental neutron diffraction pattern for comparison. (b) Among the closest configurations to starting arrangement (therefore with least amount of non-*a*, -*c*, and -*d* symmetry positions), with 11, 2, 20, 28, 2, 1 (cations on 4*a*, 4*b*, 8*c*, 8*d*, 8*e*, and 16*g* site positions, respectively), (c) 8, 1, 17, 27, 5, 6, (d) 10, 1, 17, 30, 3, 2, (e) 8, 5, 20, 21, 5, 5. Wavelength=1.66 Å.

Furthermore, the anisotropic peak at $2\theta \sim 114°$ in the experimental pattern tends to be broader than most of the equivalent peaks in simulated patterns, particularly when compared to patterns of the $Fd\bar{3}m$ system. This is indicative of strain in the material. The broadness of the peak(s) at $2\theta \sim 114°$ in diffraction patterns simulated from the $I4_1/amd$ system is closer to experiment. This is because the tetragonal split (Fig. 5) shows that some of the strain is being released by changing the lattice relative to the ideal cubic system.

The characteristics mentioned above indicate that configurations from the $I4_1/amd$ system provide a more accurate description of the structure of $\gamma$-Al$_2$O$_3$ than the $Fd\bar{3}m$ system. This is true for the experimental material examined
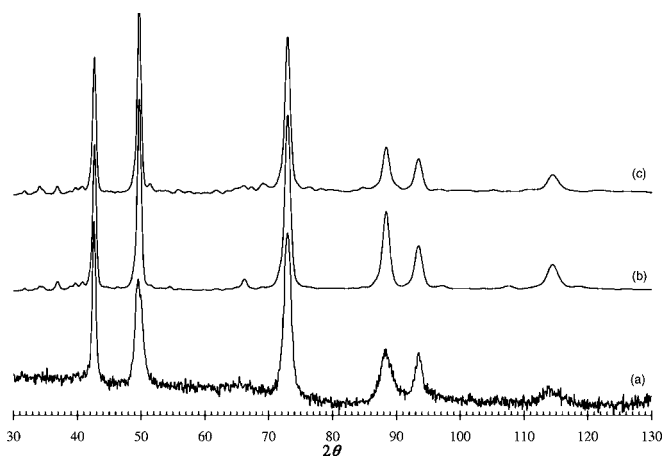


FIG. 12. Lowest energy supercell structure based on $Fd\bar{3}m$ symmetry, with 9 cations on 8*a*, 14 cations on 16*c*, 28 cations on 16*d*, and 13 cations on 48*f* site positions. (a) Experimental neutron diffraction pattern for comparison. (b) After optimization with interatomic potentials. (c) After optimizing with DFT. Wavelength =1.66 Å.

here.[22,23] However, it must be considered that the experimental diffraction pattern can vary slightly depending on the preparation conditions. For example, $\gamma$-$Al_2O_3$ synthesized from amorphous material by chemical vapor deposition (CVD) would not be expected to exhibit the same degree of anisotropic broadening, strain and preferred orientation observed here, and would have a cubic unit cell.[18,81,82] In such a case, structural configurations from the $Fd\bar{3}m$ system would provide a more appropriate description of $\gamma$-$Al_2O_3$.

In principle, it does not matter exactly which positions are occupied, as long as the same diffraction pattern is obtained. Our simulations illustrate this since we have distinct configurations that result in broadly the same diffraction pattern. Because these theoretically derived diffraction patterns have the same characteristics as those from experiment, they can be indexed in the same manner. The calculated supercells show that the overall crystal can have variations of configurations from substructure unit to substructure unit (domain structures) as long as it follows the same symmetry rules that are allowed overall (e.g., lattice dimensions, extinction rules) and have been found experimentally. The similarities in the diffraction patterns demonstrate that our optimized structures follow these rules.

The variation in the site occupancy, provided there is a reasonably consistent number of cations in $c$ symmetry positions, shows that it is more important to have cations on the appropriate Miller planes than it is to have precisely the right number of cations in particular symmetry positions. This is most easily illustrated by Figs. 11(c) and 11(e) where there are up to 23 tetrahedrally coordinated cations in the structure corresponding to Fig. 11(e) (an extreme case) but the peak intensity ratios are almost identical to those of Fig. 11(c), which corresponds to a more typical configuration.

We can also see from the modeling that, overall, the structure is ordered, but locally can have areas of varying occupancy. $\gamma$-alumina may therefore be thought of as a structure with a consistent oxygen sublattice with a varying cation configuration. Cations can be located at other site positions (non-$a$, -$c$, or -$d$ symmetry) to minimize lattice distortions, and thus the energy, locally. Distortion of octahedra and tetrahedra is present throughout the structures of both the $Fd\bar{3}m$ and $I4_1/amd$ systems. All cations were found to lie within 0.7 Å of the localized coordinate of the site positions they were situated in.

Each optimized supercell here provides a realistic example of the structure of $\gamma$-$Al_2O_3$ and the data obtained illustrates the variance in the possible cation configurations. It therefore follows that supercells described here allow for more accurate and complete modeling of the defect structure than the single unit cell approach. The single unit cell approach, namely the cubic-16$c$ or tetragonal-8$c$ models, provided in previous work[22,23] remain a valid portrayal of the structure, but provide only an average description. These models are in turn much better descriptions of the structure than the original cubic spinel description.

### E. Higher accuracy structure examples

When optimizing with DFT, the distortions of the octahedra and tetrahedra were found to reduce as the oxygen sub-

lattice was allowed to relax more freely to accommodate cation movement and the cations, generally, moved closer to the ideal positions. This distortion is a realistic feature and, coupled with the varied distribution of cations, provides direct support for the proposed short-range ordering within the interskeletal layers of $\gamma$-$Al_2O_3$ in previous work;[23] distorted octahedra and tetrahedra can occur as a consequence of the incomplete cation migration.

While the results show that almost all of the optimized structure candidates can be considered equally representative of the structure of $\gamma$-$Al_2O_3$, it is appropriate to show the most thermodynamically stable configurations. Simulated diffraction patterns for the lowest energy structures of the $Fd\bar{3}m$ and $I4_1/amd$ systems are shown in Figs. 12 and 13, respectively, which provide comparison between the DFT optimizations and those with the empirical potentials. The undulation of the background is a reflection of the oxygen sublattice being able to relax more freely to accommodate cation migration in DFT. There is little or no change in the cation positions. The relaxation of the oxygen sublattice results in the peak at $2\theta \sim 89°$ reducing in intensity and adopting an appearance closer to what is experimentally observed (Fig. 5). These structures are illustrated in Fig. 14, for optimizations where the lattice parameters have been kept fixed. The coordinates have been presented elsewhere[36] and can also be obtained through the corresponding author. The energy of these structures is 6.20 and 7.60 eV lower than the energies of the structures with configurations closest to the starting structures of the $Fd\bar{3}m$ and $I4_1/amd$ symmetry systems, respectively. The structures that have configurations among the closest to the starting structures, i.e., with the least number of occupied non-$a$, -$c$, or -$d$ site positions, are representative of the most ideal cases. When the lattice parameters of the supercells were allowed to relax during optimization, the ratios of their dimensions remained relatively constant and the structural configurations were consistent
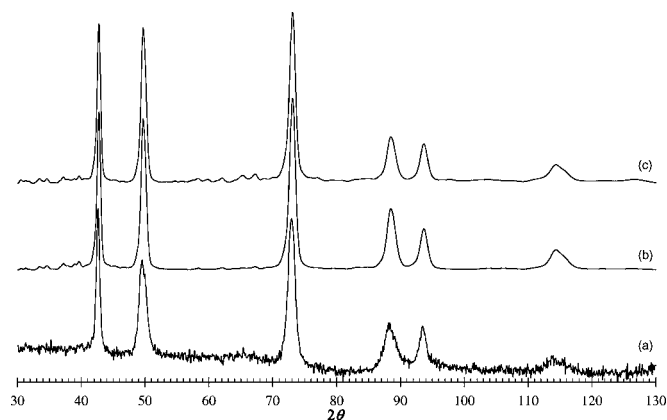


FIG. 13. Lowest-energy supercell structure based on $I4_1/amd$ symmetry, with 9 cations on 4$a$, 4 cations on 4$b$, 18 cations on 8$c$, 25 cations on 8$d$, 4 cations on 8$e$, and 4 cations on 16$g$ site positions. (a) Experimental neutron diffraction pattern for comparison. (b) After optimization with interatomic potentials. (c) After optimizing with DFT. Wavelength = 1.66 Å.
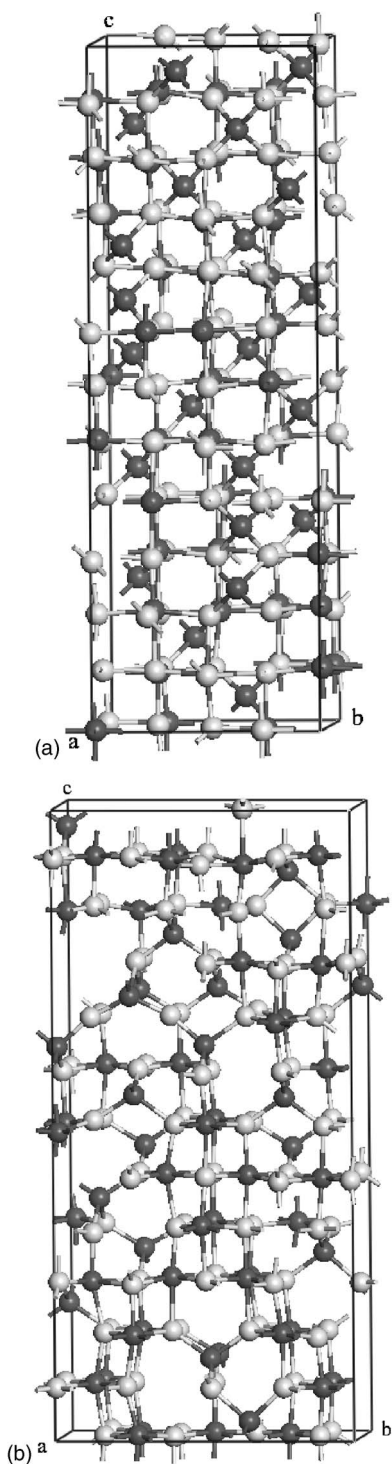
FIG. 14. Illustration of (a) $Fd\bar{3}m$ system structure represented in Fig. 12, after optimization of supercell using DFT. (b) $I4_1/amd$ system structure represented in Fig. 13, after optimization of supercell using DFT. The lighter ions are oxygen and the darker ions are Al.

with the calculations performed with fixed cell dimensions. The lowest energy structures, for example, exhibited and $a/b$ lattice parameter ratio of 0.998 for the cubic system and 2.001 for the tetragonal system.

## V. CONCLUSIONS

The purpose of this paper was to elucidate the structure of $\gamma$-$Al_2O_3$ by scrutinizing all possible structural candidates using geometric analysis before performing empirical and first principle calculations on a reduced number of structures. This was first carried out on spinel-based structural models and then on $c$ symmetry-based structural models.

Optimization of the spinel-based structural models showed that structures with some nonspinel site occupancy were more energetically favorable. However, none of the structural models exhibited a configuration close to those determined from our previous experimental studies. Nor did any of the theoretical structures yield a diffraction pattern that was characteristic of $\gamma$-$Al_2O_3$. This discrepancy between the simulated and real structures means that the spinel-based starting structure models are not close enough to the true structure of $\gamma$-$Al_2O_3$ to facilitate the derivation of its representative configuration from optimization.

However, the large number of structures which demonstrate migration of cations to $c$ symmetry positions provides strong evidence that this tendency is inherent and supports the cubic-16$c$ and tetragonal-8$c$ structure models of our previous work. It also suggests that these models are universal for crystalline $\gamma$-$Al_2O_3$.

Optimization of $c$ symmetry-based structures, with starting configurations similar to those derived from Rietveld analysis of neutron diffraction data, resulted in simulated diffraction patterns that were characteristic of $\gamma$-$Al_2O_3$. The results show that on average over 40% of the cations in the structure occupy nonspinel positions, and approximately two-thirds of these occupy $c$ symmetry positions. The similarities in the diffraction patterns show that our optimized structures follow the same symmetry rules determined by experiment. A 2:3 ratio of cations to oxygen anions was found in the subcells of most of the modelled supercells, as was an approximate 2.33:1 ratio of octahedral to tetrahedral cations in the structures. The occupancy of site positions showed variation predominantly characterized by the migration of cations away from $a$ symmetry positions to other tetrahedral sites.

The variation in the site occupancy shows that it is more important to have cations on the appropriate Miller planes than it is to have precisely the right number of cations in particular symmetry positions, provided that the number of cations on $c$ symmetry site positions remains reasonably consistent. Only when there is a significant reduction in the number of occupied $c$ symmetry site positions is there deviation of the simulated diffraction patterns away from experiment.

Overall, the average structure is ordered, but locally we can have regions of varying occupancy. The variation in the cation occupancies follows local symmetry exclusion rules. This results in the occupancy of non-$a$, -$c$, or -$d$ symmetry positions to locally minimize lattice distortions. The observed distortions in octahedra and tetrahedra, coupled with the varied distribution of cations, support the proposed short-range ordering within the interskeletal layers of $\gamma$-$Al_2O_3$ of our previous work.

The supercells described here allow for more accurate and complete modeling of the defect structure of $\gamma$-$Al_2O_3$ than the single unit cell approach. It is hoped that the data can aid in greater understanding of the transformations to other transition aluminas and the mechanisms by which applications of $\gamma$-$Al_2O_3$ function. This research also demonstrates that prior use of geometric analysis and interatomic potentials are suitable for use in investigations where stable structures need to be determined from an enormous number of possibilities. The empirical calculations delivered an acceptable level of accuracy and allowed for a comprehensive survey of possible outcomes using faster methods, before striving to achieve high accuracy for a few more likely cases.

*Currently at the Department of Physics and Astronomy, Michigan State University, Biomedical Physics Sciences Building, East Lansing, MI 48820-2320.

†Email address: A.Rohl@curtin.edu.au

[1] W. D. Kingery, H. K. Bowen, and D. R. Uhlmann, *Introduction to Ceramics*, 2nd ed. (Wiley, New York, 1976).

[2] C. N. Satterfield, *Heterogeneous Catalysis in Practice* (McGraw-Hill, New York, 1980).

[3] H. C. Stumpf, A. S. Russell, J. W. Newsome, and C. M. Tucker, Ind. Eng. Chem. **42**, 1398 (1950).

[4] B. C. Lippens and J. H. de Boer, Acta Crystallogr. **17**, 1312 (1964).

[5] P. Homsi, Third Australasian Smelter Technology Course (Sydney, Australia, 1989), p. 474.

[6] A. R. Gillespie, M. M. Hyland, and J. B. Metson, J. Met. **51**, 30 (1999).

[7] A. R. Hind, S. K. Bhargava, and S. C. Grocott, Colloids Surf., A **146**, 359 (1999).

[8] K. P. Sinha and A. P. B. Sinha, J. Phys. Chem. **61**, 758 (1957).

[9] M. Plummer, J. Appl. Chem. **8**, 35 (1958).

[10] R. Tertian and D. Papee, J. Chim. Phys. Phys.-Chim. Biol. **55**, 341 (1958).

[11] J. Harvey, H. I. Mathews, and H. Wilman, Discuss. Faraday Soc. **30**, 113 (1960).

[12] H. Yanagida and G. Yamaguchi, Bull. Mater. Sci. **35**, 1896 (1962).

[13] H. Yanagida and G. Yamaguchi, Bull. Chem. Soc. Jpn. **37**, 1229 (1964).

[14] H. Saalfeld and B. Mehrotra, Ber. Dtsch. Keram. Ges. **42**, 161 (1965).

[15] S. J. Wilson, J. Solid State Chem. **30**, 247 (1979).

[16] K. J. Morrissey, K. K. Czanderna, R. P. Merrill, and C. B. Carter, Ultramicroscopy **18**, 379 (1985).

[17] V. Jayaram and C. G. Levi, Acta Metall. Mater. **37**, 569 (1989).

[18] J. Bonevich and L. D. Marks, J. Mater. Res. **7**, 1489 (1992).

[19] Y. G. Wang, P. M. Bronsveld, and J. T. M. DeHosson, J. Am. Ceram. Soc. **81**, 1655 (1998).

[20] J. A. Wang, X. Bokhimi, A. Morales, O. Novaro, T. Lopez, and R. Gomez, J. Phys. Chem. B **103**, 299 (1999).

[21] D. Y. Li, B. H. O'Connor, G. I. D. Roach, and J. B. Cornell XVth Congress of the International Union of Crystallography (Bordeaux), Abstracts Volume C (1990).

[22] G. Paglia, C. E. Buckley, A. L. Rohl, B. A. Hunter, R. D. Hart, J. V. Hanna, and L. T. Byrne, Phys. Rev. B **68**, 144110 (2003).

[23] G. Paglia, C. E. Buckley, A. L. Rohl, K. Winter, R. D. Hart, B. A. Hunter, A. J. Studer, and J. V. Hanna, Chem. Mater. **16**, 220 (2004).

[24] R.-S. Zhou and R. L. Snyder, Acta Crystallogr., Sect. B: Struct. Sci. **47**, 617 (1991).

[25] B. K. Gan, Ph.D. thesis, School of Physical Sciences, Curtin University of Technology, Perth, 1996.

[26] B. H. O'Connor, D. Y. Li, B. K. Gan, B. Latella, and J. Carter, Adv. X-Ray Anal. **41**, 659 (1997).

[27] D. A. Dowden, J. Chem. Soc. **1**, 242 (1950).

[28] J. H. de Boer and G. M. M. Houben, Proceedings of the International Symposium on the Reactivity of Solids (Flanders Boktryckeri Aktieboolag, Göteburg, 1952), Vol. 1 p. 237.

[29] S. E. Tung and E. Mcininch, J. Catal. **3**, 229 (1964).

[30] R. M. Pearson, J. Catal. **23**, 388 (1971).

[31] S. Soled, J. Catal. **81**, 252 (1983).

[32] V. A. Ushakov and E. M. Moroz, React. Kinet. Catal. Lett. **24**, 113 (1984).

[33] A. A. Tsyganenko, K. S. S. Mirnov, A. M. Rzhevskij, and P. P. Mardilovich, Mater. Chem. Phys. **26**, 35 (1990).

[34] J. M. Saniger, Mater. Lett. **22**, 109 (1995).

[35] G. Paglia, C. E. Buckley, T. J. Udovic, A. L. Rohl, F. Jones, C. F. Maitland, and J. Connolly, Chem. Mater. **16**, 1914 (2004).

[36] G. Paglia, Ph.D. thesis, Faculty of Science, Curtin University of Technology, Perth, 2004, published online at http://adt.caul.edu.au/.

[37] J. B. Peri, J. Phys. Chem. **69**, 220 (1965).

[38] S. Blonski and S. H. Garofalini, Surf. Sci. **195**, 263 (1993).

[39] L. J. Alvarez, L.E. Leon, J. F. Sanz, M. J. Capitan, and J. A. Odriozola, J. Phys. Chem. **99**, 17872 (1995).

[40] H. Kawakami and S. Yoshida, J. Chem. Soc., Faraday Trans. **282**, 1385 (1986).

[41] M. B. Fleisher, L. O. Golender, and M. V. Shimanskaya, J. Chem. Soc., Faraday Trans. **87**, 745 (1991).

[42] H. Tachikawa and T. Tsuchida, J. Mol. Catal. A: Chem. **96**, 277 (1995).

[43] S. Cai and K. Sohlberg, J. Mol. Catal. A: Chem. **193**, 157 (2003).

[44] M. Linblad and T. A. Pakkanen, Surf. Sci. **286**, 333 (1993).

[45] O. Maresca, A. Allouche, J. P. Aycard, M. Rajzmann, S. Clemendot, and F. Hutschka, J. Mol. Struct.: THEOCHEM **505**, 81 (2000).

[46] D. A. de Vito, F. Gilardoni, L. Kiwi-Minsker, P.-Y. Morgantini, S. Porchet, A. Renkin, and J. Weber, J. Mol. Struct.: THEOCHEM **469**, 7 (1999).

[47] W. S. Xia, H. L. Wan, and Y. Chen, J. Mol. Catal. A: Chem. **138**, 185 (1999).

[48] M. Digne, P. Sautet, P. Raybaud, P. Euzen, and H. Toulhoat, J. Catal. **211**, 1 (2002).

[49] O. Maresca, A. Ionescu, A. Allouche, J. P. Aycard, M. Rajzmann, and F. Hutschka, J. Mol. Struct.: THEOCHEM **620**, 119 (2003).

[50] K. Sohlberg, S. J. Pennycook, and S. T. Pantelides, J. Am. Ceram. Soc. **121**, 10999 (1999).

[51] K. Sohlberg, S. T. Pantelides, and S. J. Pennycook, J. Am. Ceram. Soc. **123**, 26 (2001).

[52] L. J. Alvarez, J. F. Sanz, M. J. Capitan, and J. A. Odriozola, Chem. Phys. Lett. **192**, 463 (1992).

[53] F. H. Streitz and J. W. Mintmire, Phys. Rev. B **60**, 773 (1999).

[54] G. W. Watson and D. J. Willock, Chem. Commun. (Cambridge) **2001** 1076.

[55] M. H. Lee, C. F. Cheng, V. Heine, and J. Klinowski, Chem. Phys. Lett. **265**, 673 (1997).

[56] S.-D. Mo, W.-Y. Ching, and R. H. French, J. Am. Ceram. Soc. **79**, 627 (1996).

[57] K. Sohlberg, S. J. Pennycook, and S. T. Pantelides, J. Am. Ceram. Soc. **121**, 7493 (1999).

[58] C. Wolverton and K. C. Hass, Phys. Rev. B **63**, 024102 (2001).

[59] G. Gutirrez, A. Taga, and B. Johansson, Phys. Rev. B **65**, 012101 (2002).

[60] H. B. Rooksby, in *X-ray Identification and Crystal Structures of Clay Minerals*, edited by G. Brindley (Mineralogical Society, London, 1951), Chap. 10.

[61] K. S. Sickafus, J. M. Wills, and N. W. Grimes, J. Am. Ceram. Soc. **82**, 3279 (1999).

[62] L. J. Alvarez, J. F. Sanz, M. J. Capitan, M. A. Centeno, and J. A. Odriozola, J. Chem. Soc., Faraday Trans. **89**, 3623 (1993).

[63] Y. Yourdshahyan, C. Ruberto, M. Halvarsson, L. Bengtsson, V. Langer, and B. I. Lundqvist, J. Am. Ceram. Soc. **82**, 1365 (1999).

[64] G. Paglia, A. L. Rohl, C. E. Buckley, and J. D. Gale, J. Mater. Chem. **11**, 3310 (2001).

[65] H. Saalfeld, Clay Miner. Bull. **3**, 249 (1958).

[66] S. J. Wilson and J. D. C. McConnell, J. Solid State Chem. **34**, 315 (1980).

[67] *International Tables of Crystallography*, edited by T. Hahn (Kluwer, London, 1995), Vol. A.

[68] C. R. A. Catlow, R. James, W. C. Mackrodt, and R. F. Stewart, Phys. Rev. B **25**, 1006 (1982).

[69] P. P. Ewald, Ann. Phys. **64**, 253 (1921).

[70] M. P. Tosi, Solid State Phys. **16**, 1 (1964).

[71] B. G. Dick and A. W. Overhauser, Phys. Rev. **112**, 90 (1958).

[72] G. V. Lewis and C. R. A. Catlow, J. Phys. C **18**, 1149 (1985).

[73] A. Banerjee, N. Adams, J. Simons, and R. Shepard, J. Phys. Chem. **89**, 52 (1985).

[74] J. D. Gale and A. L. Rohl, Mol. Simul. **29**, 291 (2003).

[75] P. Ordejon, E. Artacho, and J. M. Soler, Phys. Rev. B **53**, R10 441 (1996).

[76] J. M. Soler, E. Artacho, J. D. Gale, A. Garcia, J. Junquera, P. Ordejon, and D. Sanchez-Portal, J. Phys.: Condens. Matter **14**, 2745 (2002).

[77] J. P. Perdew, K. Burke, and M. Ernzerhof, Phys. Rev. Lett. **77**, 3865 (1996).

[78] N. Troullier and J. L. Martins, Phys. Rev. B **43**, 1993 (1991).

[79] J. Junquera, O. Paz, D. Sanchez-Portal, and E. Artacho, Phys. Rev. B **64**, 235111 (2001).

[80] G. Paglia, C. E. Buckley, A. L. Rohl, and L. T. Byrne, J. Australas. Ceram. Soc. **38**, 92 (2002).

[81] A. L. Dragoo and J. J. Diamond, J. Am. Ceram. Soc. **50**, 568 (1967).

[82] A. Larsson and S. Ruppi, Int. J. Refract. Met. Hard Mater. **19**, 515 (2001).